

Search for a SM Higgs decaying to two photons with the ATLAS detector

M. Bettinelli*, L. Carminati, M. Consonni, G. F. Tartarelli

Dipartimento di Fisica dell'Università di Milano e I.N.F.N., Milano, Italy

L. Fayard, M. Kado, I. Koletsou, C. Reifen

LAL - Laboratoire de l'Accélérateur Linéaire

CNRS/IN2P3 - Université Paris XI, Orsay, France

M. Escalier, F. Derue, B. Laforge

LPNHE - Laboratoire de Physique Nucléaire et de Hautes Énergies

CNRS/IN2P3 - Universités Paris VI et Paris VII, France

G. Unal

CERN

Geneva, Switzerland

The search of a Standard Model Higgs boson in the two photon channel with the ATLAS detector is reviewed with a particular emphasis on the expected detector performance. The results of the inclusive analysis on fully simulated events are reported. The overall discovery potential in this channel is updated.

1 Introduction

The $H \rightarrow \gamma\gamma$ is one of the most promising discovery channels for the Standard Model Higgs boson in the low mass region ($M_H < 150$ GeV). It has been one of the benchmark channels for the LHC detectors since the early days of the project [1]. Indeed, this channel (together with the $H \rightarrow 4e$ channel) has shaped the requirements for the electromagnetic calorimetry at the LHC along the years.

The Higgs decay to two photons is a rare decay mode with a branching ratio of the order of 10^{-3} . The decay proceeds through loops with W boson or top quark. Whatever the result of the Tevatron search for the Higgs boson will be, the Higgs decay in two photons will only be accessible at the LHC due to the higher Higgs production cross section and luminosity.

*Now at Department fur Physik, Universität München (Germany).

This paper only deals with inclusive analysis, i. e. regardless of the Higgs production mechanism, which at the LHC is dominated by the gluon-gluon fusion process. Other studies have addressed the search for the two photon decay for Higgs produced via vector boson fusion [2], for Higgs produced with 0 or more jets [3] and in association with W 's, Z 's or $t\bar{t}$ pairs [4].

More recent studies have shown that other decay channels (i. e., VBF $H \rightarrow \tau\tau$) are also promising in the low mass region [5]. In any case, this channel is very appealing because of its simple and clean signature. Moreover, the closed event kinematic makes it an ideal candidate (together with $H \rightarrow 4l$ channel at higher masses) for a precise measurement of the Higgs mass due to the high energy resolution of the electromagnetic calorimetry.

In this paper we study the perspective for the ATLAS detector to observe a signal in the inclusive $H \rightarrow \gamma\gamma$ sample using simulated data. It represents an update of the results of [6] [7]. Detector and sample simulation issues affecting the measurement are studied. The study has been performed using samples simulated at the time of the ATLAS Data Challenge 1 (DC1) [8], using, in the reconstruction and analysis phases, tools and techniques available at that time.

This paper summarizes and combines the results of two ATLAS internal notes where more details can be found on some of the aspects of the analysis [9] [10] and of two additional note on more specific topics: γ /jet separation [11] and statistical significance of the observed signal [12].

2 Main ingredients of the analysis

In this section we discuss the samples used and the tools and techniques available for the analysis.

2.1 Generation and simulation of signal and background samples

For the signal, Pythia (version 6.224) [13] is used to generate events which are then fully simulated to study mass resolution and photon identification. Resbos [14] has also been used to estimate the acceptance for the gluon fusion production mode. Table 1 summarizes the generators and the corresponding cross-sections used (for a Higgs boson mass of 120 GeV). The analysis has been performed both using LO and NLO production cross-sections. The gluon fusion production cross-section comes from the HiGlu [15] package. The branching ratio to two photons is given by HDECAY[16] (0.22% at 120 GeV). More details can be found in [9].

	gg fusion	VBF production	Other production modes
LO	Pythia, 20.1 pb	Pythia, 4.2 pb	Pythia, 3.8 pb
NLO	Resbos, 36.7 pb	Pythia, 4.6 pb	Pythia, neglect NLO corrections

Table 1: Generators used and total cross-sections for the signal at a Higgs boson mass of 120 GeV.

Two different luminosity conditions are simulated corresponding to $2 \times 10^{33} \text{cm}^{-2} \text{s}^{-1}$ and $1 \times 10^{34} \text{cm}^{-2} \text{s}^{-1}$ superimposing an appropriate number of minimum bias events to the Higgs events. Electronic and pile-up noise has been added in the electromagnetic calorimeter.

The search for the $H \rightarrow \gamma\gamma$ signal at the LHC will have to deal with two sources of backgrounds: the *irreducible* background which is due to direct QCD genuine photons pair production and the *reducible* background mainly due to jets that fake photons in the calorimeter.

For the irreducible background computation, the LO analysis follows the same procedure as the one defined in the TDR (Box and Born processes from Pythia at LO multiplied by 1.5 to account for the Bremstrahlung contribution). For the NLO analysis, Diphox [17] and Resbos [18] have been used for the irreducible background computation (see [9] for a more detailed discussion on the background computations). Diphox includes all the process at order $\alpha^2\alpha_s$, including the bremstrahlung contribution with the collinear fragmentation contributions which are computed at NLO. Diphox also includes the Box (formally a $\alpha^2\alpha_s^2$) contribution at LO. The K-factor from [19] of 1.6 is applied by hand to the Diphox Box contribution to include the known higher order correction to the Box diagram (this increases the total background by around 10%). Diphox does not include resummation effect. Resbos includes Born and Box at NLO as well as the bremstrahlung contribution (but the fragmentation contribution is only at LO). Resbos also includes resummation effect. In these computations, a parton level isolation cut of 10 GeV in a cone of 0.4 is used. This was checked against the real photon identification cuts using Pythia fully simulated events. Diphox and Resbos predictions for the total irreducible background agree to better than 10% [9].

For the reducible background from di-jet events and gamma-jet events, Pythia has been used. The LO Pythia cross-sections are multiplied by a K factor of 1.7 in the NLO analysis.

2.2 Converted photons

In order to see the two photon peak above the background continuum, it is important to control each effect that can degrade the energy resolution in the electromagnetic calorimeter. During the construction and assembly of the calorimeter and ATLAS great care has been taken to minimize the effects that can compromise the energy resolution. The same care has to be taken in the calibration and the reconstruction of the events.

Converted photons pose a challenge. Converted photons are dangerous since they start showering before the beginning of the calorimeter thus degrading the energy resolution in the detector. In addition, the energy deposition in the calorimeter due to a converted photon is geometrically broader than a non converted photon. Early conversions are the most dangerous as the two electrons open up in the Inner Detector magnetic field and can be collected in two separate clusters.

If a fixed size clustering algorithm is used to reconstruct the photon energy (like in this note) a larger cluster size with respect to a non converted photon is needed. Moreover, photon/jet separation cuts, being based on the difference in cluster shape between jets and true photons should be tuned differently for converted and non-

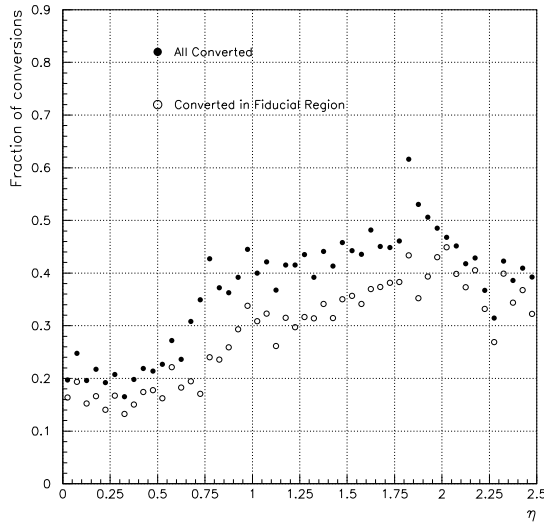


Figure 1: Photon conversion probability in the inner detector cavity (black dots) and inside the fiducial region $R < 80$ cm and $|z| < 280$ cm (open circles) as a function of η .

converted photons.

It has been estimated that about 40 % of Higgs events ($M_H = 120$ GeV) have at least one of the two photons converted with a conversion vertex within $R < 80$ cm and $|z| < 280$ cm. The probability of conversions as a function of η is shown in Fig. 1.

Conversions need to be identified and handled accordingly. Past ATLAS studies showed that it should be possible to reconstruct conversions by vertexing pair of opposite sign tracks reconstructed in the Inner Detector [20]. The algorithm used at that time (actually a combination of two algorithms for the reconstruction of early — $R < 40$ cm — and late — $R > 40$ cm — conversions) showed an efficiency of about 80 %, fairly independent on η and p_T .

As no photon conversion finder algorithm was available at the time of this note, we decided to identify conversions by looking at the Montecarlo information directly. Only conversions occurring in the fiducial region $R < 80$ cm and $|z| < 280$ cm were tagged as conversion and, among these, we applied a 80% efficiency (independent of photon η , p_T and conversion radius) in agreement with the results cited above.

2.3 Photon energy calibration

The reconstruction and offline calibration of photon energy has been studied using single photon events (mainly $E=100$ GeV photons). A set of calibration constants has been obtained that successively have been applied to the Higgs photons.

The calibration proceeds as follows. First of all each calorimeter cell is calibrated using a *normalization factor* (λ) which equalizes the cells response to a common electromagnetic scale. The λ factor is calculated equalizing the calorimeter response (sum of the energy over all the cells for a single photon hitting the calorimeter) to the deposited energy.

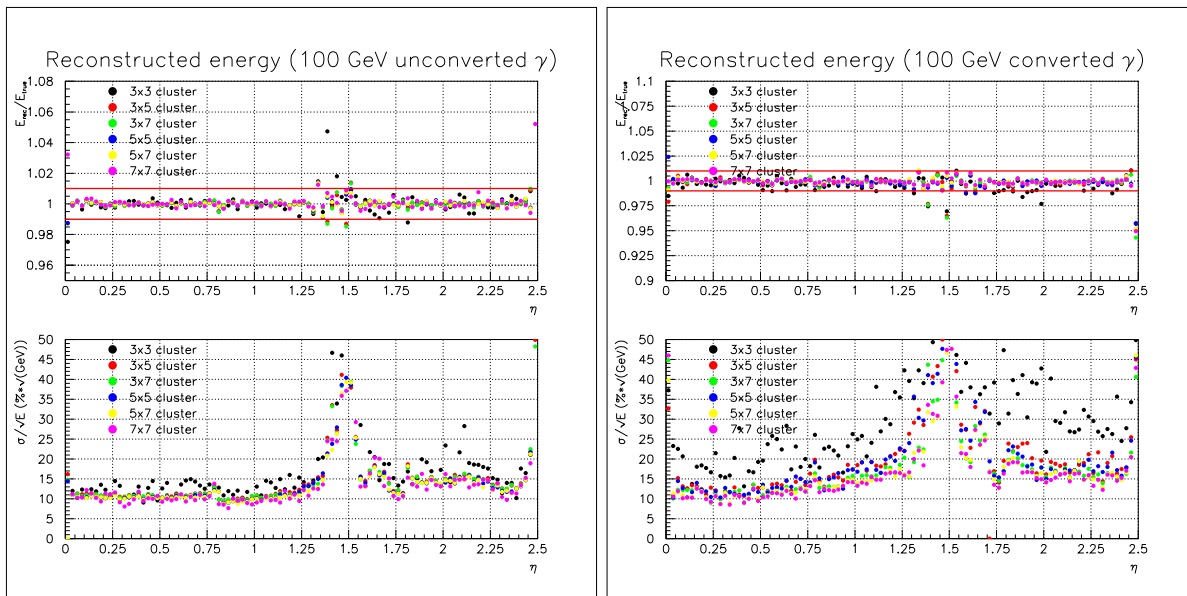


Figure 2: Reconstructed to true energy ratio (upper plots) and energy resolution σ/\sqrt{E} (lower plots) for 100 GeV unconverted (left) and converted (right) photons for different cluster sizes. The red lines on the reconstructed energy plots delimit the $\pm 1\%$ band.

Once cells have been calibrated, a sliding window algorithm is used to search for clusters. The clusters are built in different sizes in the $\eta - \phi$ coordinates in order to use the optimal dimension for a given physics analysis.

To correct for the energy lost by an incoming particle in the material in front of the calorimeter and for the longitudinal leakage, appropriate weights for the presampler and back compartments of the calorimeter have been introduced. The weights have been determined minimizing the relative energy resolution $\sigma(E_{tot})/\langle E_{tot} \rangle$. As the calculation is performed on the energy released in all calorimeter cells by single photons, the weights are independent from the cluster size. Different sets of weights for converted and unconverted photons have been produced.

Clusters are then corrected for a series of effects. The out-of-cone coefficients correct for the energy not collected into the cluster. The ϕ -modulation coefficients correct for the modulation of the energy with respect to the impact point inside each cell due to the calorimeter accordion shape. The η -modulation coefficients correct for the dependence of the energy with respect to the impact point inside the cell. This effect is due to the finite cluster size and to the fact that the shower is not fully contained inside the cluster (the effect is larger for small cluster sizes). In both cases the coefficients, which are η dependent, have been determined by fitting the observed energy shape with appropriate functions. In Fig. 2 the ratio of the energy reconstructed using this calibration procedure to the true energy for 100 GeV photons is shown; the figure also shows the energy resolution σ/\sqrt{E} .

The energy dependence of all the coefficients determined in this calibration scheme has been found, at first order, to be negligible for the photon energy range used in this analysis. This scheme satisfies all the requirements for the ATLAS calorimetry but

one. The linearity, in fact, starts degrading at low photon energy (less than 20 GeV). This is one of the reason why this scheme has been improved [21] and other calibration strategies [22] are under study. However, as the minimum photon energy cut in this analysis is 25 GeV (see Sec. 3), the effect has no impact on this analysis.

2.4 Photon/jet separation

Powerful photon identification is required to reject the background from jets faking photons (from di-jet events and gamma-jet events) significantly below the irreducible background. The photon identification relies on the fine segmentation of the electromagnetic calorimeter, especially the first layer, allowing an event-by-event rejection of "isolated" π^0 , which is the main source of fake prompt photons from jets. Track isolation cuts are also applied to reduce further the fake background.

The study of photon-jet separation is based on fully simulated di-jet events and Higgs events [11]. Two different luminosity conditions are simulated corresponding to $2 \times 10^{33} \text{cm}^{-2} \text{s}^{-1}$ and $1 \times 10^{34} \text{cm}^{-2} \text{s}^{-1}$. For the low (high) luminosity sample, the hard-scattering cut in the Pythia di-jet sample is 17 GeV (25 GeV). In addition, a particle level filter is applied before simulation, requiring a least 17(22) GeV transverse energy in a window of $\Delta\eta \times \Delta\phi = 0.12 \times 0.12$.

The following variables are used to distinguish direct photons from jets:

- Hadronic leakage, defined as the ratio of the transverse energy reconstructed in a window $\Delta\eta \times \Delta\phi = 0.2 \times 0.2$ in the first compartment of the hadronic calorimeter to the transverse energy of the cluster reconstructed in the electromagnetic calorimeter.
- Lateral shower shape variables in the second sampling of the EM calorimeter: $R_\eta(37)$ and $R_\phi(33)$, given by the ratio of the energy reconstructed in a 3×7 cluster to the energy in a 7×7 cluster and the ratio of the energy reconstructed in a 3×3 cluster to the energy in a 3×7 cluster respectively.
- Lateral width in η in the second sampling of the EM calorimeter, computed in a window of 3×5 cells, corrected for the impact point dependence within the cell.
- Search for a second maximum in the energy deposition in the first sampling (strips) of the EM calorimeter, giving the variable $\Delta E = E_{\text{max2}} - E_{\text{min}}$, difference between the energy associated with the second maximum E_{max2} and the energy reconstructed in the strip with the minimal value between the first and second maxima E_{min} , and the variable $\tilde{E}_{\text{max2}} = E_{\text{max2}} / (1 + 9 \times 10^{-3} E_T) [\text{GeV}]$, where E_T is the transverse energy of the cluster in the electromagnetic calorimeter and the constant value 9 has units GeV^{-1}
- F_{side} , the fraction of energy deposited outside the shower core of three central strips, calculated from the following formula : $F_{\text{side}} = [E(\pm 3) - E(\pm 1)] / E(\pm 1)$, where $E(\pm n)$ is the energy deposited in $\pm n$ strips around the strip with the highest energy

- $\omega_{3\text{strips}}$, the shower width over three strips around the one with the maximal energy deposit.

Cuts on these variables are defined in bins of η :

- $|\eta| \leq 0.75$;
- $0.75 < |\eta| \leq 1.37$;
- $1.52 < |\eta| \leq 1.8$;
- $1.8 < |\eta| \leq 2.0$;
- $2.0 < |\eta| \leq 2.37$.

The cuts on the variables are tuned to obtain an efficiency of approximately 80%, independent of pseudo-rapidity η . Cut thresholds are chosen to be as close as possible to the edge of the photon distributions. The details of the cuts applied at the calorimeter level at low and high luminosity can be found in [11].

The same cuts are applied for converted and unconverted photons. Studies [23] of the γ - π^0 separation have shown that if conversions can be identified efficiently, different cuts can be applied for converted and unconverted photons, which would allow an increase by 10-20% of the rejection for the same overall efficiency.

After the calorimeter cuts, the contamination of the inclusive signal from charged hadrons is greatly reduced. The remaining background is dominated by low multiplicity jets containing high- p_T π^0 mesons. After the application of the cuts on the shower shape in the first section of the EM calorimeter, this background cannot be reduced using only the cluster shower shape information. Indeed most of the surviving π^0 are either very asymmetric decays, or decays with a small opening in η (less than one strip). On the other hand, only 70% of the parton energy is found in the cluster energy. There is thus a non negligible amount of hadronic activity around the cluster which can be used to increase the rejection. In the following, we will use a cut on track isolation using the information from the inner detector.

The variable defined for the track isolation is the sum of the p_T of all tracks with $\Delta R < 0.3$ (ΔR is the $\eta - \phi$ distance between the track parameters at the vertex and the cluster position). One should keep in mind that in the reconstruction applied to the DC1 samples, there is an effective cut-off on the track p_T which is close to 2 GeV/ c . In order not to include in this variable the tracks coming from photon conversion, some additional selections are applied to tracks with $\Delta R < 0.1$:

- the impact parameter must be less than 0.01 cm.
- the track p_T must not exceed 15 GeV/ c (to remove tracks from very asymmetric conversions).
- the track must not have a partner forming a photon conversion candidate. A partner is the closest track in $\cot(\theta)$ of opposite sign such that:
 - $|\Delta\cot(\theta)| < 0.05$;
 - the distance of closest approach between the two circles of the track trajectories in the transverse plane is less than 0.15 cm;
 - the radius of the point of closest approach is less than 100 cm.

The cut that has been applied on this isolation variable is 2.5 GeV/c at low luminosity and 4 GeV/c at high luminosity. The efficiency for a photon from Higgs decay is approximately 96%, the rejection factor against jets fulfilling all previous cuts is around 1.6-1.7.

In addition, the Level1 calorimeter cuts are also applied to the simulated events.

The identification efficiency ε_γ for photons at low and high luminosity is detailed in Table 2 over the full rapidity range $|\eta| < 2.37$. The inter-cryostat region (crack) of the calorimeters in the range $1.37 < |\eta| < 1.52$ is excluded.

ε_γ (in %)	low luminosity	high luminosity
Hadronic calorimeter	97.74 ± 0.12	97.80 ± 0.12
second layer of electromagnetic calorimeter	91.62 ± 0.23	94.24 ± 0.19
first layer of electromagnetic calorimeter	83.68 ± 0.31	85.25 ± 0.30
Tracks Isolation	80.13 ± 0.33	79.22 ± 0.30
LVL1 trigger	79.99 ± 0.33	78.62 ± 0.34

Table 2: Photon identification efficiency ε_γ of $H \rightarrow \gamma\gamma$ photons in the offline analysis at low and high luminosity. The crack in the electromagnetic calorimeter $1.37 < |\eta| < 1.52$ is excluded.

The total efficiency ε_γ is $\sim 80\%$ at low luminosity and $\sim 78\%$ at high luminosity. Fig. 3 shows the efficiency as a function of pseudo-rapidity (left) and transverse momentum (right). The efficiency is lower for converted photons because their showers start earlier and are thus broader in the calorimeter (this effect is also increased in the ϕ direction by the magnetic field). However, these photons are also the ones for which the energy is less well measured, so this is not necessarily a bad feature. The efficiency also increases slightly with p_T .

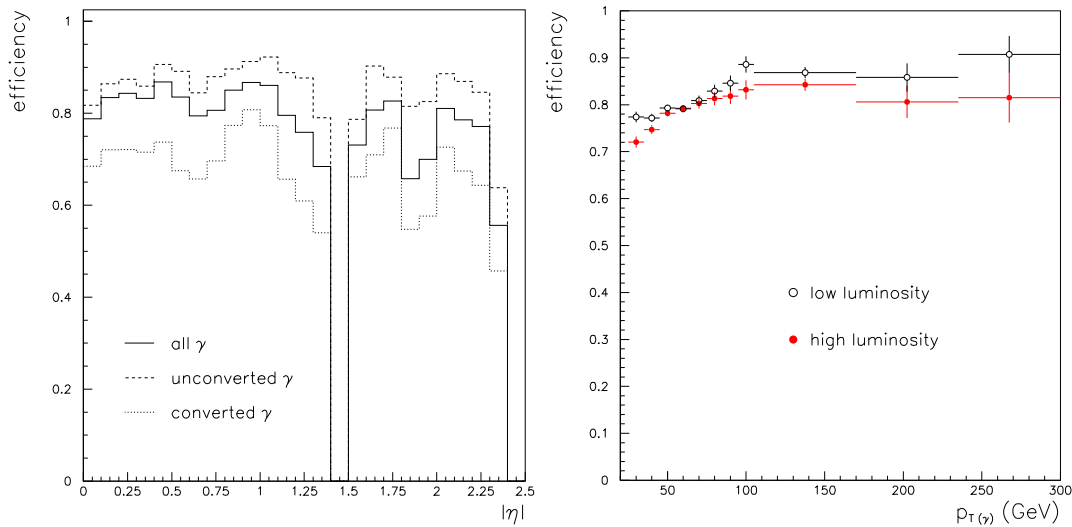


Figure 3: Efficiency as a function of pseudo-rapidity (left, at low luminosity) and transverse momentum (right, at both low and high luminosity).

The rejection is normalised with respect to the number of jets according to the formula: $R = N(\text{jets})/N(\text{fake } \gamma)$. The jets are reconstructed with the fast simulation program ATLFAST starting with the unfiltered generated sample. Uncorrected ATLFAST jets have been used. The number of jets above 20 (25) GeV in the η fiducial range is 0.335 (0.167) per generated event in the low luminosity (17 GeV parton level cut) sample. In the high luminosity sample (25 GeV parton level cut) there are 0.539 jets above 25 GeV per generated event. The total statistics analysed corresponds to 13.245×10^6 generated events in the low luminosity sample and 9.450×10^6 generated events in the high luminosity sample.

True direct photons or photons from quark Bremsstrahlung, which are present in the jet sample, are not included in the number of "fake" photons, as these backgrounds are included in the "irreducible" background for the Higgs search and estimated separately.

Tab. 3 details the rejection factors against QCD jets obtained after each step of the analysis at low and high luminosity, with the number of π^0 remaining after each cut. The first layer of the electromagnetic calorimeter enables a reduction in this number by a factor of about 2-3. The rejections are given before and after the LVL1 cuts are applied. Before an explicit isolation cut is applied offline, the isolation cut applied at LVL1 increases the rejection by 15-40% depending on the sample. The effect of the LVL1 cuts is significantly smaller when track isolation cuts are applied: it is about 5% in the low luminosity sample and around 15% in the high luminosity sample.

After all cuts, the rejection is 4760 (6680) for $p_T > 20 (> 25)$ GeV at low luminosity and 4930 for $p_T > 25$ GeV at high luminosity.

The rejection can be evaluated as a function of p_T by taking the ratio of the $p_T(\text{jet})$ and the $p_T(\text{photon candidate})$ spectra (see Fig. 4). In principle, since a given $p_T(\text{photon})$ can come from a full spectrum of jet p_T this curve cannot be directly applied to any sample having a jet spectrum different from the one of the inclusive jets. A more detailed procedure to deconvolute the jet spectrum has also been performed for the evaluation of the fake background in the Higgs search [11].

The rejection curve as a function of the transverse momentum is shown in Fig. 5. The rejection is shown for all jets at both luminosities (left) as well as for gluon- and quark-initiated jets separately at low luminosity (right). Clusters and jets are defined as coming from a quark or a gluon using the type of the highest energy parton in a cone of 0.4. The gluon jet rejection is higher than the quark jet rejection by a factor of about 5-7 due to the lower probability of fragmentation of gluons to π^0 carrying a large fraction of the original parton momentum: for $p_T > 25$ GeV/ c in the low luminosity sample, the rejection after the isolation cut is 2880 ± 190 for quark jets and 20650 ± 2370 for gluon jets. More details on this difference can be found in [11].

The study of photon/jet separation shows that it is possible to achieve a rejection on QCD jets of the order of 5000 while maintaining an overall efficiency of about 80%, including track isolation cuts.

	low luminosity			high luminosity		
	$0 < \eta < 2.37$	barrel	end-cap	$0 < \eta < 2.37$	barrel	end-cap
# of unfiltered Atlfast jets	2.203×10^6	1.445×10^6	0.758×10^6	5.095×10^6	3.326×10^6	1.769×10^6
hadronic calorimeter	166 ± 1 (2999 π^0)	146 ± 1 (2022 π^0)	215 ± 4 (977 π^0)	116 ± 1 (8632 π^0)	101 ± 1 (5649 π^0)	152 ± 1 (2983 π^0)
2 nd layer EM calorimeter	864 ± 17 (1583 π^0)	801 ± 19 (1072 π^0)	1004 ± 37 (511 π^0)	573 ± 6 (4758 π^0)	508 ± 6 (3257 π^0)	741 ± 16 (1501 π^0)
1 st layer EM calorimeter	3340 ± 130 (435 π^0)	3150 ± 150 (289 π^0)	3680 ± 260 (146 π^0)	2170 ± 40 (1419 π^0)	1920 ± 50 (994 π^0)	2840 ± 110 (425 π^0)
(+ LVL1 trigger)	3920 ± 170 (370 π^0)	3770 ± 190 (240 π^0)	4170 ± 310 (130 π^0)	3050 ± 80 (1023 π^0)	2820 ± 80 (684 π^0)	3670 ± 160 (339 π^0)
track isolation (no trigger)	6260 ± 330 (214 π^0)	6170 ± 400 (131 π^0)	6370 ± 580 (83 π^0)	4220 ± 120 (709 π^0)	3860 ± 130 (473 π^0)	5030 ± 270 (236 π^0)
LVL1 trigger	6680 ± 370 (214 π^0)	6750 ± 460 (131 π^0)	6480 ± 600 (83 π^0)	4930 ± 160 (610 π^0)	4650 ± 180 (395 π^0)	5510 ± 310 (215 π^0)

Table 3: Rejection factors after successive cuts. Rejections are normalised to jets with $p_T > 25$ GeV at both low and high luminosity. Results are given for the whole η range as well as for barrel ($|\eta| < 1.4$) and end-cap regions ($1.4 < |\eta| < 2.5$). The crack in the electromagnetic calorimeter $1.37 < |\eta| < 1.52$ is excluded. The numbers in brackets are the number of π^0 remaining after the cuts.

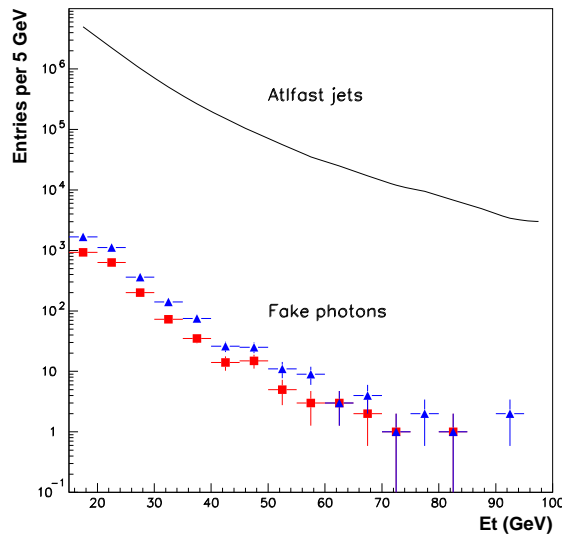


Figure 4: p_T spectra of the Atlfast jets and the fake photon candidates before (blue triangles) and after (red squares) the track isolation cut in the low luminosity jet sample. The Atlfast jets spectrum has been evaluated from the unfiltered events.

2.5 Photon direction

In order to reduce the contribution of the angular term to the mass resolution, the photon direction must be known with good accuracy.

The shower barycenter in the η coordinate is measured separately in the various electromagnetic calorimeter compartments. The measurements from the strips and

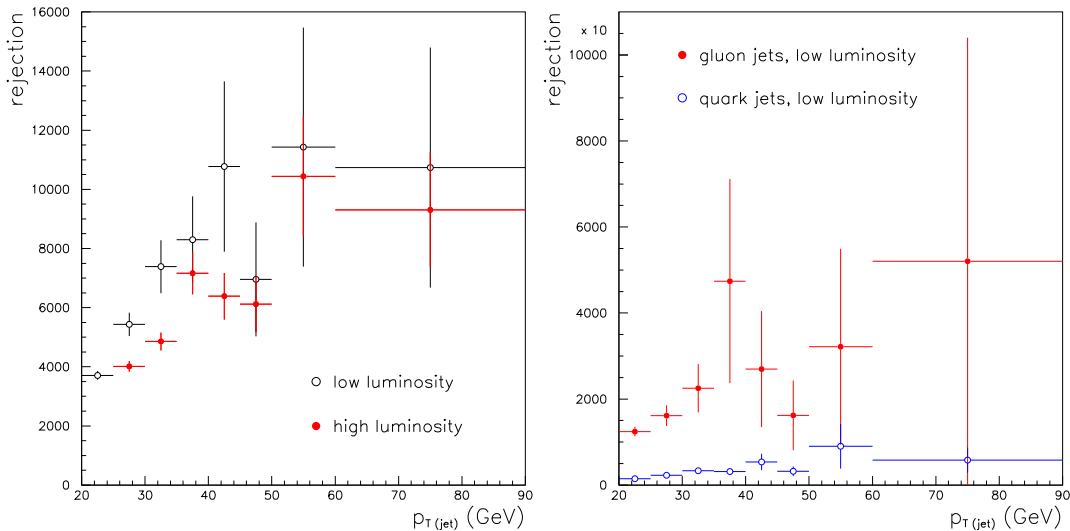


Figure 5: Jet rejection as a function of transverse momentum for all jets at low and high luminosity (left), and for gluon and quark jets separately at low luminosity (right). All cuts including track isolation and LVL1 requirement are applied

middle compartments are used to extract a global η value: a higher weight is given to the strips which have a higher intrinsic resolution due to the finer granularity. Due to the finite granularity of the detector, especially in the second sampling, the difference between the true and the computed barycenter as a function of the position inside the cell has a typical S-shape. In the offline version used in this note (7.0.2), correction functions were determined using 100 GeV photons (for strips and middle compartments and separately for barrel and end-cap), by fitting the observed shapes with an appropriate function.

The cluster position in ϕ is determined from the energy barycenter in the second sampling only which exhibits the best granularity along this direction. The ϕ position measure is affected by an η -dependent offset that needs to be corrected for. The offset is due to the accordion shape and depends on the beginning of the middle compartment with respect to the folds of the accordion. Along η the offset follows the strips-middle segmentation on the electrodes. The correction has been obtained using $E_T = 60$ GeV photons.

These algorithms, however, assume that the γ 's are coming from the nominal interaction vertex assumed to coincide with the center of the ATLAS detector. At the LHC the interaction point will be known with good accuracy only in the transverse plane ($\sigma_{x,y} = 15 \mu\text{m}$) while in the z direction the vertex will have a spread of about $\sigma_z = 5.6$ cm. This spread along the beam line direction compromises the Higgs mass resolution if not corrected for. So it is necessary to reconstruct the position of the primary vertex along the beam direction and recompute each photon direction with respect to the new vertex. As the two Higgs photons do not provide any charged track that can be reconstructed in the Inner Detector, the primary vertex has to be determined from the tracks produced with the Higgs boson. If photons convert and the converted tracks are iden-

tified and reconstructed in the Inner Detector, they can provide additional direction information

The presence of pile-up obviously complicates the situation. The presence of additional interaction vertices from minimum bias interaction (about 2.3 at low luminosity and 23 at high luminosity) might lead to the association of the Higgs photons to a wrong vertex. In this case a series of cuts usually based on the vertex track multiplicity and/or on the $\sum p_T$ of the tracks at the vertex are needed to select the right vertex. However, these cuts depend on the Higgs p_T spectrum and on the characteristic of the underlying events and of the minimum bias events at the LHC. These issues have not been addressed in this note.

On the other hand, the calorimeter allows a stand-alone measurement of the γ direction thanks to its longitudinal division in three samplings, although with a worse resolution than the one provided using charged tracks. Particularly important is the first sampling with its fine subdivision along η in 4-mm wide strips.

Results have been obtained for the two extreme cases. In the first case, an *a priori* knowledge of the primary vertex position and a resolution of $\sigma_z = 40 \mu\text{m}$ is assumed as to mimic a 100 % efficient reconstruction of the primary vertex using charged tracks (see [24]). In the second case, information from the calorimeter is used. The first case is used at low luminosity (where it is a bit optimistic as the effect of low luminosity pile-up is neglected) and the second one is used at high luminosity (and the results might be a bit pessimistic as the information provided by the Inner Detector is not fully deployed).

In both cases the η direction of each Higgs photon has been recomputed from a χ^2 fit in the R-Z plane applied to the η values measured in the strips, middle and presampler (the presampler is used where available: $|\eta| < 1.8$) calorimeter layers with the additional constraint of a primary vertex from the Inner Detector (first case only). Moreover, if a conversion has been assumed to be reconstructed the conversion vertex (if the conversion radius is less than 40 cm) is included into the fit, with the expected Inner Detector resolutions (0.03 cm for conversion radii less than 20 cm and 0.54 cm for radii up to 40 cm [25]).

3 Results

The tools and techniques described in the previous section have been applied to the Higgs events. Photons have been identified using the cuts described in Sec. 2.4. Conversions are handled as discussed in Sec. 2.2. A 3×7 cluster has been used for converted photons to recover some of the energy that might be lost due to the opening of the two electrons in the magnetic field; for unconverted photons a 3×5 (5×5) cluster is used in the barrel (endcap). The chosen cluster sizes are a compromise between containment and noise.

In the simulation all the effects that contribute to the calorimeter resolution constant term [26], which by design needs to be kept at the level of 0.7%, are not fully taken into account. Assuming that the simulation accounts only for a constant term of about $c_{sim} = 0.3\%$ [27], a constant term $c_{reco} = 0.63\%$ has been introduced in the analysis (so that $c = c_{sim} \oplus c_{reco} = 0.7\%$) by smearing the reconstructed photons energy.

For the simple inclusive analysis, the same cuts as in [7] are used:

- Transverse momentum of the photons above 25 GeV.
- At least one photon with transverse momentum above 40 GeV.
- η of both photons in the fiducial range: $0 < |\eta| < 1.37$ or $1.52 < |\eta| < 2.37$

3.1 Vertex and Mass resolutions

The mass resolution of the photon pairs has been determined from an asymmetric gaussian fit ($[-2\sigma, +3\sigma]$) of the invariant mass peak. The asymmetric window is used to reduce the impact of the residual low energy tails in the distribution. The results are shown in Table 4 at low luminosity and in Table 5 for high luminosity. The mass window for the evaluation of the signal significance (for brief, the *mass bin* in the following) has been defined as $\pm 1.4 \sigma$ around the central value.

Tables 4 and 5 also show the resolution on the primary vertex at low and high luminosity. If the Inner Detector vertex is included in the fit (Tables 4), the resolution is dominated by the vertex resolution that can be obtained using charged tracks. At high luminosity neither any information on the primary vertex that can be obtained using the Inner detector nor the conversion information has been used for the vertex resolution quoted in Table 5. If the conversion information is used, for events with at least one conversion, the vertex resolution decreases to about 0.2 mm.

	120 GeV	130 GeV	140 GeV
vertex resolution (mm)	0.039	0.040	0.040
mass resolution (GeV)	1.36	1.42	1.51

Table 4: Primary vertex resolution, mass resolutions, acceptance in mass bin at low luminosity (Inner Detector primary vertex measure included in the direction reconstruction algorithm) for different Higgs boson masses.

	120 GeV	130 GeV	140 GeV
vertex resolution (mm)	15.9	16.2	15.6
mass resolution (GeV)	1.59	1.65	1.70

Table 5: Primary vertex resolution, mass resolutions, acceptance in mass bin at high luminosity (direction reconstruction from calorimeter information only) for different Higgs boson masses.

The results are also shown in Figures. 6 and 7. The vertex resolution plot at low luminosity simply reproduces the ID vertex resolution that has been assumed and shows that the fit procedure does not introduce any significant bias. The tails at high masses in the mass plots are due to events with poorly reconstructed primary vertices. This

also affects the low mass tails which are however largely dominated by events with at least one conversion. In this category we find early conversions that despite the use of a larger cluster size are not fully contained and true converted photons that we have handled as unconverted (to mimic the expected inefficiency of the conversion finder algorithm).

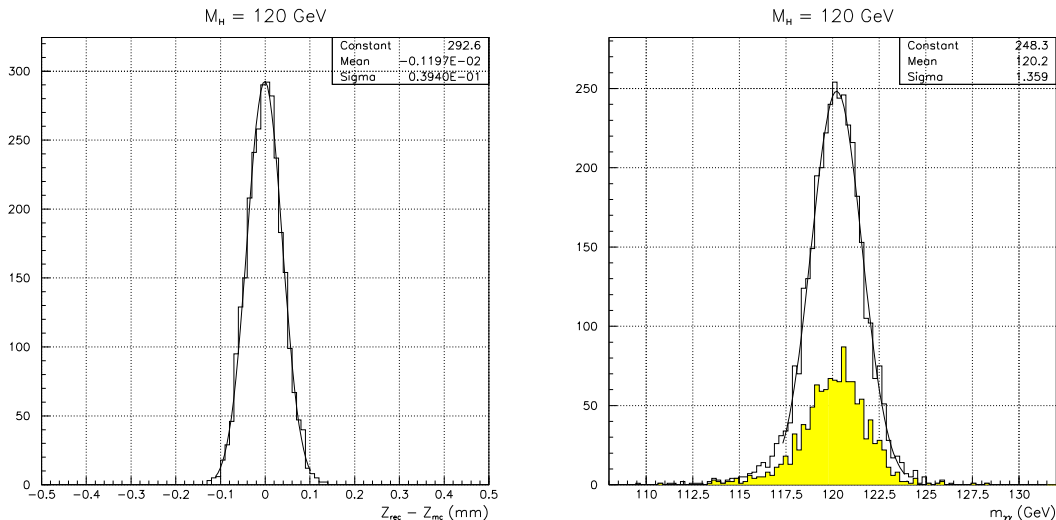


Figure 6: Primary vertex resolution (left) and mass resolution (right) for $M_H = 120 \text{ GeV}$ in Higgs boson events at low luminosity, including ID vertex information. In the mass plot, the white histogram contains all selected events and the yellow one contains the subsample of events with at least one converted photon.

3.2 Discovery potential

Table 6 summarizes the rate of events inside a mass window of $\pm 1.4\sigma$ for 30 fb^{-1} of data taken in low luminosity conditions, using LO normalisations for the signal and background. The statistical significance is computed using only statistical uncertainties. Table 7 shows the results for the same luminosity but this time using NLO normalizations for the signal and the background. Table 8 shows the significances at LO and NLO for 100 fb^{-1} of data taken in the high luminosity conditions.

The signal rate is estimated from the signal cross-section, the branching ratio and the total acceptance in the mass window (acceptance of the kinematical cuts times photon identification efficiency times fraction of events inside $\pm 1.4\sigma$ around the true mass). The irreducible background rate is computed from Resbos taking into account the photon identification efficiency for a mass window of $\pm 1.4\sigma$. The reducible background is computed applying to Pythia jet-jet or photon-jet events the parameterization of the jet rejection factor. The difference between quark and gluon initiated jet is taken into account. This is important because jets in the photon-jet events are mostly quark jets, for which the rejection power is smaller.

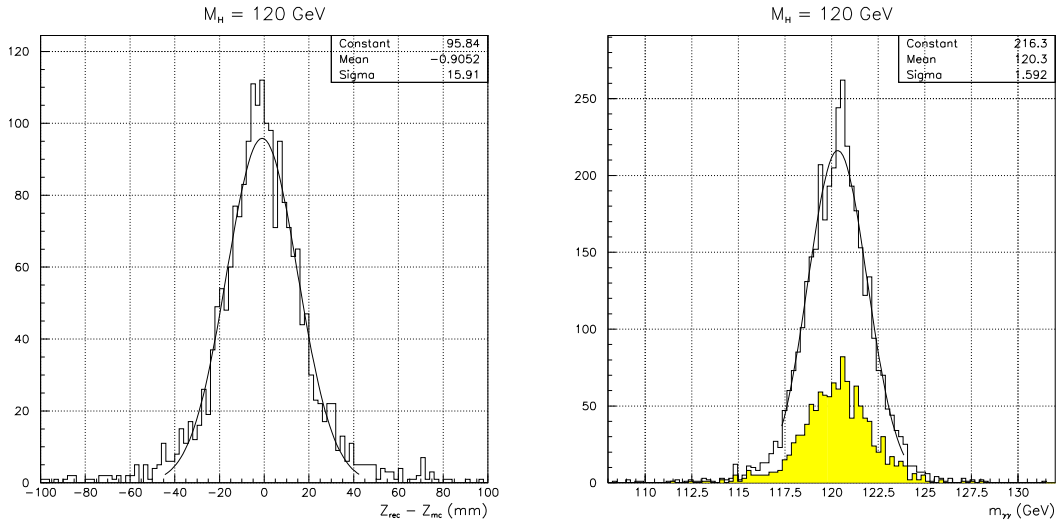


Figure 7: Primary vertex resolution (left) and mass resolution (right) for $M_H = 120 \text{ GeV}$ in Higgs boson events at high luminosity using calorimeter information only (ID vertex and conversions not included in the fit). In the mass plot, the white histogram contains all selected events and the yellow one contains the subsample of events with at least one converted photon.

Higgs Mass (GeV)	120	130	140
Signal	551	430	375
Irreducible Bkg	9211	7475	6073
Jet-Jet Bkg	354	325	284
Photon-Jet Bkg	1979	1672	1387
Total Background	11544	9472	7744
Significance	4.8	4.4	4.3

Table 6: Rates for 30 fb^{-1} using LO normalizations

Figure 8 shows one example of mass distribution of a pseudo-experiment with 30 fb^{-1} , for an assumed Higgs boson mass of $120 \text{ GeV}/c^2$, using the NLO normalizations.

These estimates for the signal and especially the background suffer from large uncertainties, so the absolute values for the significances should be taken with a grain of caution. It should however be noted that the background will be known much better with the data using the mass sidebands. Preliminary studies [12] show that fitting the background mass spectrum from the sidebands leads to a $\approx 10\%$ decrease in the significance compared to a situation where the background in the mass window is perfectly known. Some improvements to the simple inclusive analysis can probably be achieved by dividing data into categories of difference mass resolutions.

It is also possible to significantly improve the discovery potential adding discriminating variables in the analysis. Two kinematical variables were investigated in [9]:

Higgs Mass (GeV)	120	130	140
Signal	815	758	610
Irreducible Bkg	14100	11472	12391
Jet-Jet Bkg	603	553	483
Photon-Jet Bkg	3364	2843	2356
Total Background	18067	14868	12391
S/\sqrt{B}	6.1	6.2	5.4

Table 7: Rates for 30 fb^{-1} using NLO normalizations

Higgs Mass (GeV)	120	130	140
S/\sqrt{B} LO	8.0	7.1	6.9
S/\sqrt{B} NLO	9.8	10.1	8.9

Table 8: Rates for 100 fb^{-1} using NLO normalizations

the total transverse momentum of the photon pair and the polar angle of the photon in the center of mass of the two photon system. Figure 9 shows the predicted distributions from Resbos (for the dominant gluon-gluon fusion signal and the irreducible background) and Pythia (for the other background components and the reducible backgrounds). To exploit this discriminating power, a likelihood for the signal and the background is computed and events are weighted by the likelihood ratio S/B . Signal events have then a higher weight than background events and this leads to an increase in the signal significance. This increase is $\approx 30\%$. Again, the exact value of this increase depends on the modelling of the shapes for the background. This should be determined in-situ using mass sidebands. This study shows however that there is room for a significant improvement in the inclusive analysis.

4 Conclusions

The discovery potential of the $H \rightarrow \gamma\gamma$ decay mode from a simple inclusive analysis has been re-evaluated using DC1 data. Compared to the TDR, a small worsening of the mass resolution is seen, because of the increase in material upstream the calorimeter. The photon identification capabilities are similar but, for this study, differences between quark and gluon initiated jets have been taken into account, which increases the fake background from gamma-jet events. Isolation cuts have been applied to keep this background significantly below the irreducible background. The rates of signal and irreducible background have been estimated both in a “conservative” LO analysis, and in a full NLO analysis for signal and background. As expected, the discovery potential is significantly increased if NLO rates are used. The expected significance is 6.1 for 30 fb^{-1} of data for a Higgs mass of 120 GeV. The use of discriminating variables based on the event kinematics has been investigated and found to be promising. Given the uncertainties in our absolute predictions of the level of irreducible background, ex-

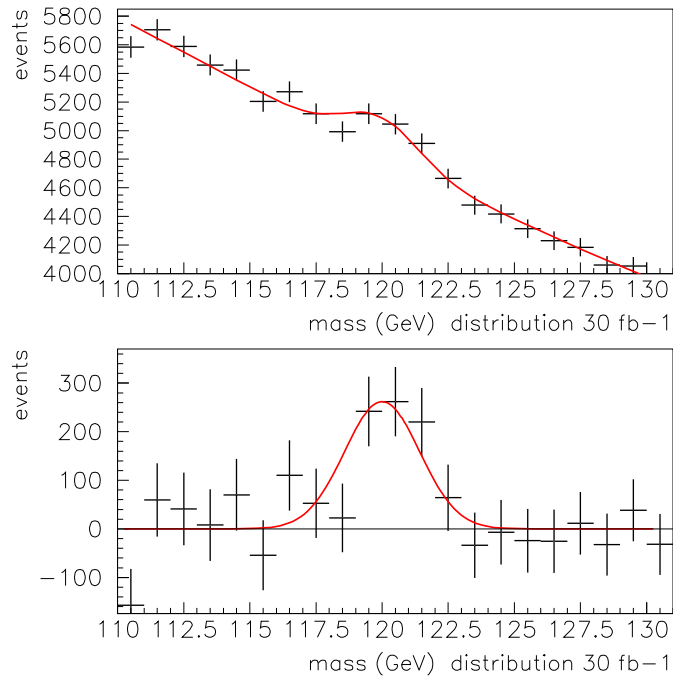


Figure 8: Example of observed mass distribution before (top) and after (bottom) background subtraction, for a pseudo-experiment with 30 fb^{-1} and a Higgs mass of $120 \text{ GeV}/c^2$

act significance numbers have to be taken with a grain of caution. However, it seems very likely that this channel offers a good discovery potential at low luminosity in the mass range 110-140 GeV.

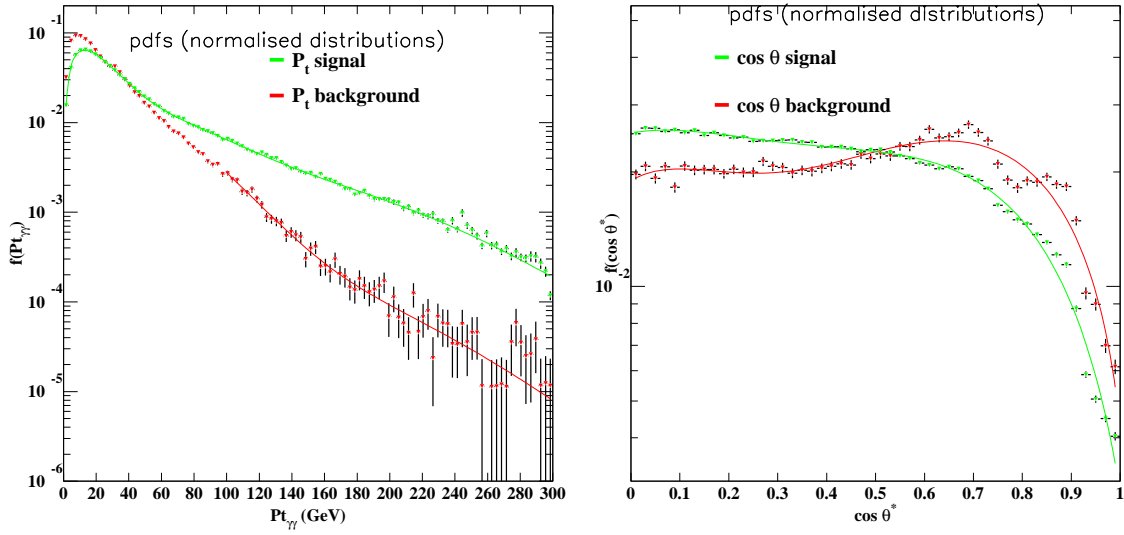


Figure 9: $P_{T\gamma\gamma}$ and $\cos \theta^*$ distributions of the signal and background, for a Higgs boson mass of 120 GeV. All kinematical cuts are applied but a loose mass window cut (from 100 to 160 GeV).

References

- [1] The ATLAS Collaboration, ATLAS Technical Proposal for a General-Purpose pp experiment at the Large Hadron Collider at CERN, CERN/LHCC/94-43, Sec. 11.2.
- [2] K. Cranmer *et al.*, Prospects for Higgs Searches via VBF at the LHC with the ATLAS Detector, hep-ph/0401148.
- [3] S. V. Zmushko, Search for $H \rightarrow \gamma\gamma$ in association with jets, ATL-PHYS-99-014.
S. V. Zmushko, Search for $H \rightarrow \gamma\gamma$ in association with one jet, ATL-PHYS-2002-020.
- [4] The ATLAS Collaboration, ATLAS Detector and Physics Performance Technical Design Report, CERN/LHCC/99-15, Sec. 19.2.2.2.
- [5] S. Asai *et al.*, Prospects for the Search of a Standard Model Higgs Boson in ATLAS using Vector Boson Fusion, J. Phys. G 28 (2002) 2453-2474.
- [6] The ATLAS Collaboration, ATLAS Detector and Physics Performance Technical Design Report, CERN/LHCC/99-14, Sec. 7.8.1.
- [7] The ATLAS Collaboration, ATLAS Detector and Physics Performance Technical Design Report, CERN/LHCC/99-15, Sec. 19.2.2.
- [8] R. Sturrock *et al.*, A Step Towards a Computing Grid for the LHC Experiments: ATLAS Data Challenge 1, CERN-PH-EP-2004-028 (2004).
- [9] M. Escalier *et al.*, Search for a Standard Model Higgs boson in the ATLAS experiment on the $H \rightarrow \gamma\gamma$ channel, ATL-PHYS-INT-2006-002.
- [10] M. Bettinelli, L. Carminati, M. Consonni, G. F. Tartarelli, Analysis of the inclusive $H \rightarrow \gamma\gamma$ channel with DC1 samples, ATL-PHYS-PUB-2006-016.
- [11] M. Escalier, F. Derue, L. Fayard, M. Kado, B. Laforge, C. Reifen, G. Unal, Photon/jet separation with DC1 data, ATL-PHYS-PUB-2005-018.
- [12] I. Koletsou, G. Unal, L. Fayard, Preliminary study of S/\sqrt{B} in Higgs to $\gamma\gamma$, ATL-PHYS-INT-2006-003.
- [13] T. Sjostrand *et al.*, Comput. Phys. Comm. 135 (2001) 238.
- [14] C. Balazs and C. P. Yuan, Phys. Rev. D 59 (1999) 114997.
- [15] M. Spira, hep-ph/9510357.
- [16] A. Djouadi *et al.*, Comput. Phys Comm. 108 (1998) 56.
- [17] T. Binoth *et al.*, Eur. Phys. J. C 16 (2000) 311.
- [18] C. Balasz *et al.*, Phys. Lett. B 489 (2000) 157.

- [19] Z. Bern, L. Dixon and C. Schmidt, Phys. Rev. D 66 (2002) 074018.
- [20] The ATLAS Collaboration, ATLAS Detector and Physics Performance Technical Design Report, CERN/LHCC/99-14, Sec. 7.5.1.
- [21] B. Mellado, S. Paganis, W. Quayle, S. Wu, Electron-based longitudinal weights for the ATLAS EM Barrel Calorimeter and shower isolation studies with an application to the $H \rightarrow ZZ^{(*)} \rightarrow 4e$ analysis, ATL-CAL-2004-002.
- [22] M. Aharrouche *et al.*, Energy linearity and resolution of the ATLAS electromagnetic barrel calorimeter in an electron test-beam, Nucl. Instr. and Methods in Phys. Res. A 568 (2006) 601–623.
- [23] C.Reifen *et al.*, γ/π^0 separation in the 1st compartment of the ATLAS EM calorimeter with DC2 data, ATLAS-PHYS-INT-2005-005.
- [24] The ATLAS Collaboration, ATLAS Detector and Physics Performance Technical Design Report, CERN/LHCC/99-14, Sec. 3.6.1.
- [25] The ATLAS Collaboration, ATLAS Inner Detector Technical Design Report, CERN/LHCC/97-16, Sec. 6.3.2.2.
- [26] The ATLAS Collaboration, ATLAS Detector and Physics Performance Technical Design Report, CERN/LHCC/99-14, Sec. 4.3.6.
- [27] The ATLAS Collaboration, ATLAS Calorimeter Performance, CERN/LHCC/96-40 (1996), Sec. 2.6.1.